Supporting Information for

Antenna-coupled infrared nano-spectroscopy of intra-molecular vibrational interaction

R. Wilcken, J. Nishida, J.F. Triana, A. John-Herpin, H. Altug, S. Sharma, F. Herrera, and M.B. Raschke

roland.wilcken@colorado.edu, felipe.herrera.u@usach.cl, markus.raschke@colorado.edu

This PDF file includes:

Supporting Information Text

Experiment

Preparation of nanoantennas. IR-resonant gold nanoantennas are fabricated as described previously (1) on a CaF_2 substrate coated by 100 nm thick Au layer followed by 90 nm MgF_2. The resulting ground plane coupling minimizes dissipation, resulting in long lived antennas with narrow linewidths of ∼80 cm^{-1} FWHM corresponding to ∼120 fs lifetimes and Q-factors of ∼29. Far-field reflection FTIR-microscope characterization is shown in Fig. S1 including the resulting parameters from Gaussian curve fitting for the center frequency ν_{ant} and the full width at half maximum linewidth (FWHM). Note that the linewidth is larger than in near-field spectroscopy because of the ensemble average over the length distribution measured in the FTIR-microscope. The spatial and spectral field characteristics of the bare and tip-coupled antennas are modeled by Finite-Difference Time-Domain (FDTD) simulation (see Fig. 2a in the main text).

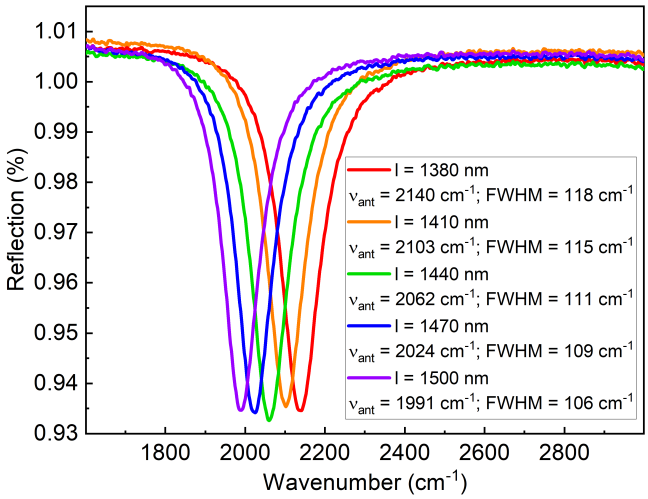

Fig. S1. Far-Field reflection measurements of selected nanoantennas with full width at half maximum (FWHM) linewidth and center frequency ν_{ant} determined by Gaussian curve fitting. The antenna length l is the nominal length targeted in fabrication.

The antennas are arranged on the chip as shown in Fig. S2. Antenna arrays are made for near-field and far-field measurements. The far-field arrays contain antennas of nominally identical length and are designed to allow for far-field ensemble measurements in a reflection FTIR-microscope (see S1). In the near-field arrays, the length of the antennas increases from one row to the next ranging from 1360 nm to 1550 nm, covering the frequency range from 1850 to 2100 cm^{-1}. This allows us to probe different antennas with only a small movement of the AFM translation stage. The distance between the antennas is chosen so that no near-field interaction occurs between antennas (∼20 μm) to ensure an isolated optical antenna response. The chip contains three types of antennas: "bright mode" antennas directly resonant at the intended frequencies, "dark mode" antennas resonant at the first overtone, and dimer antennas with a nanometer size gap between two antennas. Only the bright mode antennas are utilized in this work.

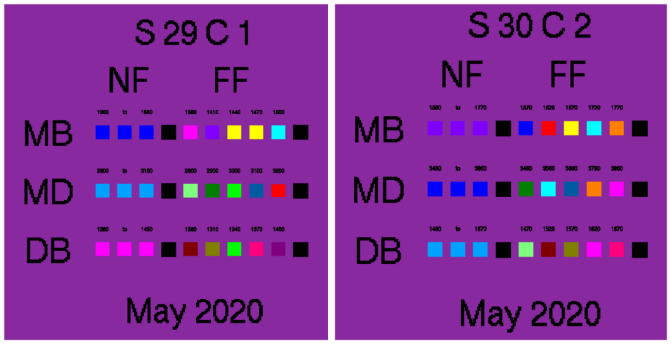

Fig. S2. Nanoantenna chip design

.

Monolayer synthesis. The Re-carbonyl complex monolayer on gold is prepared according to Ref. (2, 3). First, the gold surface is functionalized with 11-bromoundecan-1-thiol, followed by a bromide to azide (N_3^-) substitution. The rhenium complex is

functionalized at the bipyridyl ligand with a terminal alkyne. The complex is linked to the monolayer by a click reaction with the azide copper-catalyzed azide-alkyne cycloaddition (CuAAD). The sythesis is reproduced in Fig. S3. Between the steps, samples are washed with 10 mL of each dimethlyformamide and ethanol.

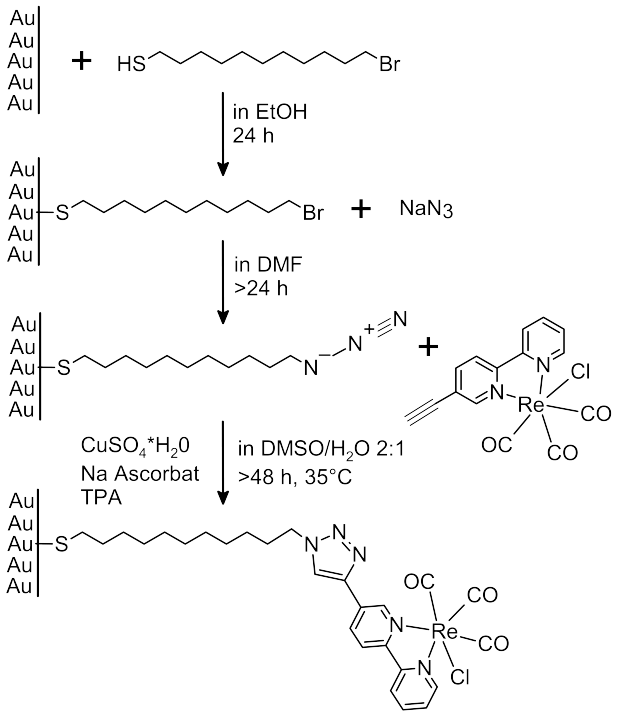

Fig. S3. Synthesis of the monolayer coating on the gold nanoantennas following Ref. (3).

Data fitting and error analysis. Here we give further explanations on the data fitting process and on the error estimates. The approach is to fit the interferograms in the time domain to retrieve the decay times $T_{\mathrm{FID,j}}$, frequencies ν_{j}, amplitudes A_{j}, and relative phases ϕ_{j} for the antenna (ant) and the two vibrational modes (A'(1), A'(E)). In contrast to previous work(4) the antenna lifetime is not modeled as instantaneous. The first step is to fix the parameters for the driving laser field by fitting a reference measurement on gold. Note that the maximum of the interferograms is delayed because of the finite antenna response (see Fig. 2b). We define the reference field as follows

$$E_{\mathrm{ref/in}}(t) = A_{\mathrm{L}} \exp(-2\ln 2 \frac{(t-t_0)^2}{\mathrm{FWHM}^2}) \exp(i\omega_0 t), \qquad [1]$$

with the scaling amplitude A_{L}, the FWHM pulse duration (typical pulse durations are 170 fs) and ω_0 the center frequency of the pulse.

Having the laser parameters constrained, the measurements of the antenna are fitted, which have been measured under the same conditions. Typically, we kept the vibrational frequencies ($\bar{\nu}_{\mathrm{A'(1)}} = 2028$ cm^{-1} and $\bar{\nu}_{\mathrm{A'(E)}} = 1919$ cm^{-1}) fixed as determined independently and the antenna lifetime $T_{\mathrm{FID,ant}}$ within a reasonable range.

Table S1. Fit parameters and values for four antennas of different lengths averaged over five consecutive scans at the same position on the antenna. Nominal antenna length and the antenna frequency $\bar{\nu}_{\mathrm{ant}}$, the antenna lifetime $T_{\mathrm{FID,ant}}$, the vibrational lifetime $T_{\mathrm{FID,A'(1)}}$, the amplitude ratio between the vibrational and the antenna signal $A_{\mathrm{A'(1)}}/A_{\mathrm{ant}}$, the phase difference between vibration and antenna $\phi_{\mathrm{A'(1)}} - \phi_{\mathrm{ant}}$, the vibrational lifetime $T_{\mathrm{FID,A'(E)}}$, the amplitude ratio between the vibrational and the antenna signal $A_{\mathrm{A'(E)}}/A_{\mathrm{ant}}$ and the phase difference between vibration and antenna $\phi_{\mathrm{A'(E)}} - \phi_{\mathrm{ant}}$. The vibrational frequency is fixed to $\bar{\nu}_{\mathrm{A'(1)}} = 2028$ cm^{-1}. The parameters for the laser field are identical for this dataset with a laser frequency of $\bar{\nu}_{\mathrm{Laser}} = 2013$ cm^{-1} and a FWHM pulse duration of $t = 167$ fs, which we assume to possess no significant chirp. Individual values are the average of fit parameters from 5 consecutive scans.

Length (nm)	$\bar{\nu}_{\mathrm{ant}}$ (cm^{-1})	$T_{\mathrm{FID,ant}}$ (fs)	$A_{\mathrm{A'(1)}}/A_{\mathrm{ant}}$ (arb. units)	$T_{\mathrm{FID,A'(1)}}$ (fs)	$\phi_{\mathrm{A'(1)}} - \phi_{\mathrm{ant}}$ (rad)	$A_{\mathrm{A'(E)}}/A_{\mathrm{ant}}$ (arb. units)	$T_{\mathrm{FID,A'(E)}}$ (fs)	$\phi_{\mathrm{A'(E)}} - \phi_{\mathrm{ant}}$ (rad)
1400	2022 ± 1	129 ± 2	0.22 ± 0.01	379 ± 6	2.5 ± 0.1	-	-	-
1440	1978 ± 1	152 ± 3	0.046 ± 0.01	683 ± 16	0.74 ± 0.05	0.24 ± 0.02	250 (fixed)	2.9 ± 0.1
1460	1970 ± 1	179 ± 1	0.043 ± 0.002	561 ± 16	0.54 ± 0.01	0.35 ± 0.02	250 (fixed)	3.1 ± 0.1
1520	1937 ± 1	120 (fixed)	0.019 ± 0.001	516 ± 33	0.68 ± 0.1	0.76 ± 0.04	250 (fix)	2.5 ± 0.1

In Tab. S1, resulting parameters for antennas of different length are shown. Five consecutive scans at the same position on the antenna are made and averaged after fitting. The fit values are highly reproducible with a small variance. For consistency, we compare values as measured on the terminal of the antenna facing the incoming light pulse. We find a higher variance between different antennas within the same fabrication badges. In Tab. S2 we compare fit results on four antennas of nominally identical length that give us an estimate of the variance for the fit parameters.

Table S2. Fit parameters and values for four individual measurements on the same nominal antenna length to determine the variance between different antennas (averaged over five consecutive scans per antenna). Nominal antenna length, the antenna frequency ν_{ant}, the antenna decay time $T_{\mathrm{FID,ant}}$, the vibrational decay time $T_{\mathrm{FID,A'(1)}}$, the amplitude ratio between the vibrational and the antenna signal $A_{\mathrm{A'(1)}}/A_{\mathrm{ant}}$ and the phase difference between vibration and antenna $\phi_{\mathrm{A'(1)}} - \phi_{\mathrm{ant}}$.

Length (nm)	$\bar{\nu}_{\mathrm{ant}}$ (cm^{-1})	$T_{\mathrm{FID,ant}}$ (fs)	$A_{\mathrm{A'(1)}}/A_{\mathrm{ant}}$ (arb. units)	$T_{\mathrm{FID,A'(1)}}$ (fs)	$\phi_{\mathrm{A'(1)}} - \phi_{\mathrm{ant}}$ (rad)
1400	2022	129	0.22	379	2.5
1400	2025	140	0.47	254	2.4
1400	2023	135	0.28	332	3.6
1400	2020	133	0.36	247	2.0
	average	134 ± 5	0.34 ± 0.11	379 ± 63	2.64 ± 0.68

Monolayer on gold surface. In order to determine the intrinsic vibrational lifetime of a monolayer of the Re-carbonyl complex, a sample on a pure gold surface is prepared. Nano-FTIR measurements are performed as described in the main text that result in the interferometric timetraces as shown in Fig. S4. The vibrational signal is weaker compared to the IR-nanoantenna enhanced case, as expected. Using the same fitting procedure as described above, a decay time of $T_{\mathrm{FID,A'(1)}} = 750 \pm 150$ fs is determined. For an excitation frequency of 1911 cm^{-1}, a decay time of $T_{\mathrm{FID,A'(E)}} = 315 \pm 75$ is determined (see Fig. S5).

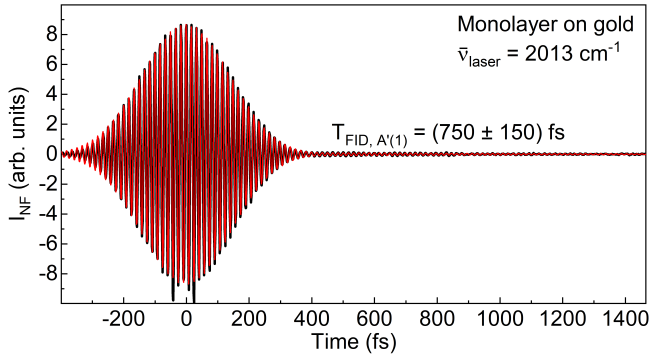

Fig. S4. Nano-FTIR measurement of the Re-carbonyl complex on a gold surface to determine the intrinsic FID lifetime of the A'(1) mode. Excitation at 2013 cm^{-1}.

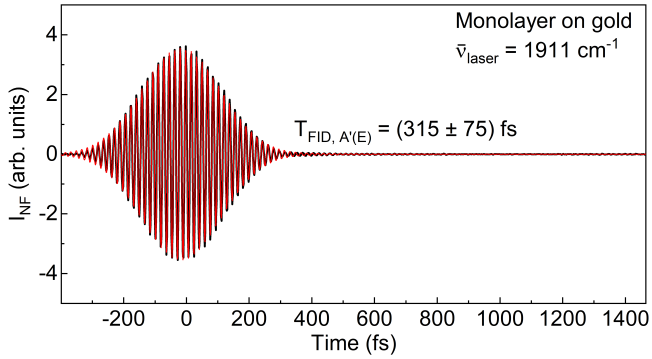

Fig. S5. Nano-FTIR measurement of the Re-carbonyl complex on a gold surface to determine the intrinsic FID lifetime of the A'(E) mode. Excitation at 1911 cm^{-1}.

FID fitting and FT spectra. Data with fits to combined antenna, laser and vibrational components, as well as the respective Fourier transform spectra can be found in Fig. S6 and Fig. S7 for the 1440 nm antenna. This dataset corresponds to Fig. 3b in the main text. The same representation can be found in Fig. S8 and Fig. S9 for the 1520 nm antenna (Fig. 3c in the main text).

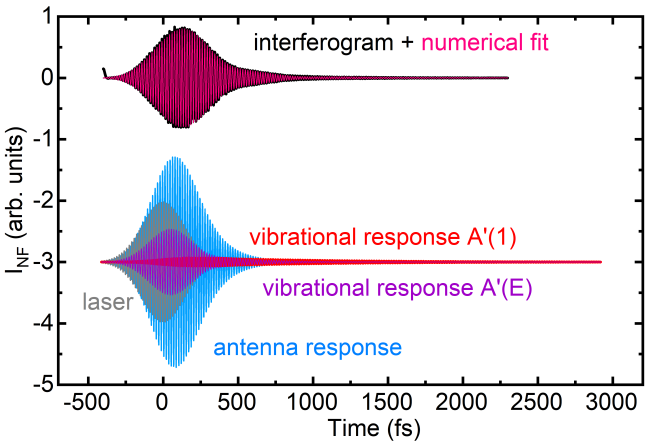

Fig. S6. Interferogram measured at the right antenna terminal of a 1440 nm long antenna (top, black) with model fit (top, magenta), and decomposed (bottom) into the driving laser field (grey), the antenna response (blue), and vibrational response of A′(1)(red) and A′(E)(violet) modes.

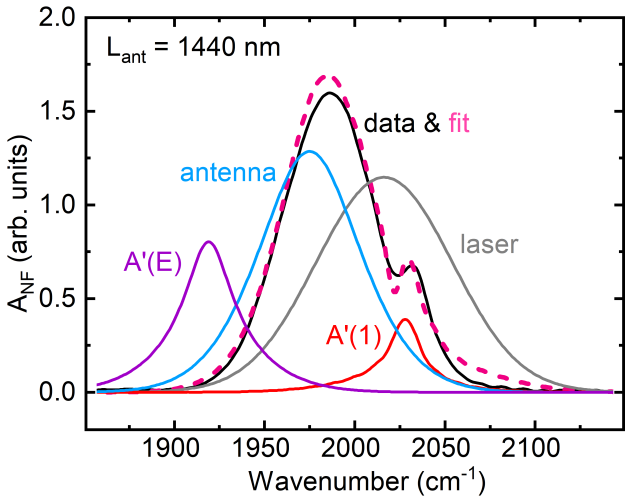

Fig. S7. Fourier-transform of time-domain signals for the 1440 nm long antenna from Fig. S6. Spectra shown for the data (black) with model fit (magenta), and the individual spectra for the driving laser field (grey), the antenna response (blue), and vibrational response of A′(1) (red) and A′(E) (violet) modes from the fit.

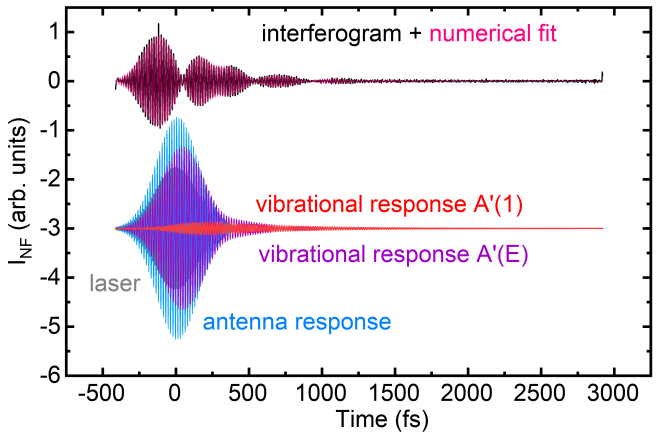

Fig. S8. Interferogram measured at the right antenna terminal of a 1520 nm long antenna (top, black) with model fit (top, magenta), and decomposed (bottom) into the driving laser field (grey), the antenna response (blue), and vibrational response of A′(1) (red) and A′(E) (violet) modes.

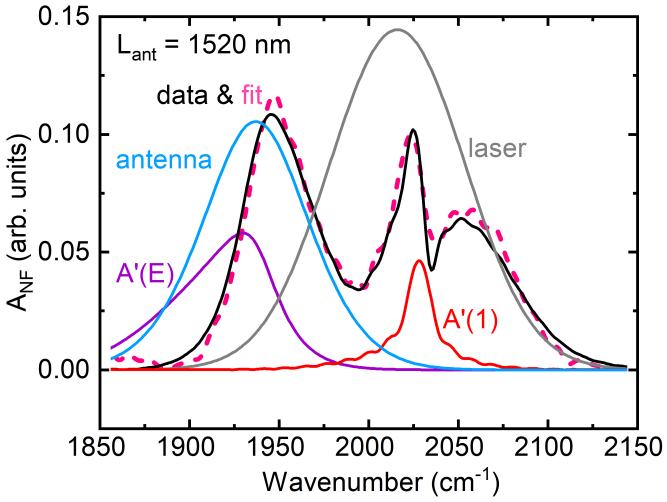

Fig. S9. Fourier-transform of time-domain signals for the 1520 nm long antenna from Fig. S8. Spectra shown for the data (black) with model fit (magenta), and the individual spectra for the driving laser field (grey), the antenna response (blue), and vibrational response of A′(1) (red) and A′(E) (violet) modes from the fit.

Lifetime comparison with literature. In the following Table S3, we compare literature values for the homogeneous and inhomogeneous linewidth of the A'(1) vibrational mode and the respective decay times for the population T_1, pure dephasing T_2^* and dephasing due to inhomogeneous broadening with values from our work. The enhancement due to antenna coupling accelerates the T_1 time (see main text for details).

Theory

Lindblad quantum master equation. We model the monolayer as an ensemble of N molecular vibrations that couple to the antenna field with collective couplings strength $g_K = \sqrt{N} g_k$, where g_k is the coupling of mode k of an individual molecular vibration. We consider two vibrational modes coupled to the antenna field, which are the modes A'(1) (symmetric) and the effective mode A'(E)=A'(2)+A" (asymmetric), as shown in Fig. 1 of the main text. In the collective mode approximation (5), the ensemble of molecular vibrations is represented by the collective operators $\hat{B}_{\rm S}$ and $\hat{B}_{\rm A}$, for the symmetric mode at $\omega_{\rm S} = 2028.0\ {\rm cm}^{-1}$ and the effective asymmetric mode at $\omega_{\rm A} = 1919.0\ {\rm cm}^{-1}$, respectively. The effective light-matter Hamiltonian is given by

$$\hat{\mathcal{H}} = \omega_{\rm ant}\hat{a}^\dagger\hat{a} + \omega_{\rm S}\hat{B}_{\rm S}^\dagger\hat{B}_{\rm S} + \omega_{\rm A}\hat{B}_{\rm A}^\dagger\hat{B}_{\rm A} + [g_{\rm S}(\hat{a}\hat{B}_{\rm S}^\dagger + \hat{a}^\dagger\hat{B}_{\rm S}) + g_{\rm A}(\hat{a}^\dagger\hat{B}_{\rm A} + \hat{a}\hat{B}_{\rm A}^\dagger)] + \zeta_{\rm SA}(\hat{B}_{\rm S}\hat{B}_{\rm A}^\dagger + \hat{B}_{\rm S}^\dagger\hat{B}_{\rm A}), \quad [2]$$

where $\hat{a}$ is the single mode field operator for an antenna resonance frequency $\omega_{\rm ant}$, $\zeta_{\rm SA}$ is the bilinear coupling strength between two vibrational modes, $g_{\rm S}$ and $g_{\rm A}$ are the collective light-matter couplings of the symmetric and asymmetric modes with the antenna field, respectively.

Table S3. Comparison of literature values for the Re-carbonyl monolayer A'(1) mode with values measured in this work with and without antenna coupled enhancement. For the population lifetime T_1, the homogeneous linewidth Γ_{hom}, the pure dephasing time T_2^*, the inhomogeneous linewidth Γ_{inhom}, the dephasing time by inhomogeneous broadening T_{inhom}, the total linewidth Γ_{total} and the corresponding FID time T_{FID}. Green indicates that the value was calculated from the values given in the respective reference. Blue indicates that the value is the average of the respective literature values. Red indicates changes due to antenna coupling. *Calculated from decay time / Measured linewidth. TD: Measured directly in the time domain. FD: Calculated from spectral linewidth.

Source	T_1 (ps)	Γ_{hom} (cm^{-1})	T_2* (ps)	Γ_{inhom} (cm^{-1})	T_{inhom} (fs)	Γ_{total} (cm^{-1})	T_{FID} (fs)
Rosenfeld et al. (2)	10	1.8	8.5	14.3	742	15.2	699 (FD)
Yan et al. (3)	11	3.2	4	17.9	536	21	506 (FD)
This work (uncoupled)	10.5	2.5	6.3	16.1	640	14/16*	750 (TD) / 665 (FD)
This work (coupled)	0.3	30	6.3	16.1	640	30	330 (TD)

We derive the equations of motion by solving the Lindblad quantum master equation (6)

$$\frac{\mathrm{d}}{\mathrm{d}t}\hat{\rho}_{\mathrm{S}} = -i[\hat{\mathcal{H}}' + \hat{H}_{\mathrm{F}}(t), \hat{\rho}_{\mathrm{S}}] + \mathcal{L}_{\kappa_{\mathrm{ant}}}[\hat{\rho}_{\mathrm{S}}] + \mathcal{L}_{\gamma_{\mathrm{S}}}[\hat{\rho}_{\mathrm{S}}] + \mathcal{L}_{\gamma_{\mathrm{A}}}[\hat{\rho}_{\mathrm{S}}], \quad [3]$$

where $\hat{\rho}_{\mathrm{S}}$ is the reduced density matrix of the coupled system and $[\hat{A}, \hat{B}]$ denotes a commutator. The driving over the antenna is given by

$$\hat{H}_{\mathrm{F}}(t) = F_{\mathrm{d}}(t)\left[\hat{a}\mathrm{e}^{i\omega_{\mathrm{L}}t} + \hat{a}^{\dagger}\mathrm{e}^{-i\omega_{\mathrm{L}}t}\right], \quad [4]$$

where $F_d(t) = F_0\varphi(t)$ is proportional to the square root of the photon flux of the laser pulse at frequency ω_{L}, and $\varphi(t)$ is the carrier envelope of the laser pulse. The Lindblad superoperators that describe dissipation and decoherence are given by

$$\mathcal{L}_{\kappa_{\mathrm{ant}}}[\hat{\rho}_{\mathrm{S}}] = \frac{\kappa_{\mathrm{ant}}}{2}\left(2\hat{a}\hat{\rho}_{\mathrm{S}}\hat{a}^{\dagger} - \hat{a}^{\dagger}\hat{a}\hat{\rho}_{\mathrm{S}} - \hat{\rho}_{\mathrm{S}}\hat{a}^{\dagger}\hat{a}\right) \quad [5]$$

$$\mathcal{L}_{\gamma_{\mathrm{S}}}[\hat{\rho}_{\mathrm{S}}] = \frac{\gamma_{\mathrm{S}}}{2}\left(2\hat{B}_{\mathrm{S}}\hat{\rho}_{\mathrm{S}}\hat{B}_{\mathrm{S}}^{\dagger} - \hat{B}_{\mathrm{S}}^{\dagger}\hat{B}_{\mathrm{S}}\hat{\rho}_{\mathrm{S}} - \hat{\rho}_{\mathrm{S}}\hat{B}_{\mathrm{S}}^{\dagger}\hat{B}_{\mathrm{S}}\right) \quad [6]$$

$$\mathcal{L}_{\gamma_{\mathrm{A}}}[\hat{\rho}_{\mathrm{S}}] = \frac{\gamma_{\mathrm{A}}}{2}\left(2\hat{B}_{\mathrm{A}}\hat{\rho}_{\mathrm{S}}\hat{B}_{\mathrm{A}}^{\dagger} - \hat{B}_{\mathrm{A}}^{\dagger}\hat{B}_{\mathrm{A}}\hat{\rho}_{\mathrm{S}} - \hat{\rho}_{\mathrm{S}}\hat{B}_{\mathrm{A}}^{\dagger}\hat{B}_{\mathrm{A}}\right), \quad [7]$$

where κ_{ant} is the photon decay rate of the antenna mode and γ_{S}, γ_{A} are the vibrational relaxation rates of the symmetric and effective asymmetric modes, respectively.

From Eq. (3), the equations of motion for the mean field coherences are given by

$$\langle\dot{\hat{B}}_{\mathrm{S}}\rangle = -(\gamma_{\mathrm{S}}/2 + i\omega_{\mathrm{S}})\langle\hat{B}_{\mathrm{S}}\rangle - ig_{\mathrm{S}}\langle\hat{a}\rangle - ig_{\mathrm{L}}\langle\hat{B}_{\mathrm{A}}\rangle \quad [8]$$

$$\langle\dot{\hat{a}}\rangle = -(\kappa_{\mathrm{ant}}/2 + i\omega_{\mathrm{ant}})\langle\hat{a}\rangle - ig_{\mathrm{S}}\langle\hat{B}_{\mathrm{S}}\rangle - ig_{\mathrm{A}}\langle\hat{B}_{\mathrm{A}}\rangle - iF_{\mathrm{d}}(t)\mathrm{e}^{-i\omega_{\mathrm{L}}t} \quad [9]$$

$$\langle\dot{\hat{B}}_{\mathrm{A}}\rangle = -(\gamma_{\mathrm{A}}/2 + i\omega_{\mathrm{A}})\langle\hat{B}_{\mathrm{A}}\rangle - ig_{\mathrm{A}}\langle\hat{a}\rangle - ig_{\mathrm{L}}\langle\hat{B}_{\mathrm{S}}\rangle, \quad [10]$$

where $\langle\hat{B}_{\mathrm{S}}\rangle$ is the symmetric A'(1) mode coherence, $\langle\hat{a}\rangle$ is the antenna field coherence, and $\langle\hat{B}_{\mathrm{A}}\rangle$ is the asymmetric A'(E) effective coherence.

We use the bare vibrational and antenna bandwidths (FWHM) to set the values of the bare material and photonic decay rates. In the Lorentzian response theory used here the decay times are calculated by $T^0_{2,\mathrm{vib}}(\mathrm{fs}) = 10610.4 \div \gamma_{\mathrm{vib}}(\mathrm{cm}^{-1})$. Similarly $T^0_{2,\mathrm{ant}}(\mathrm{fs}) = 10610.4 \div \kappa_{\mathrm{ant}}(\mathrm{cm}^{-1})$. The model parameters g_{S}, g_{S}, ζ_{SA} are then calibrated to match the measured values of $T_{\mathrm{FID,A'(1)}}$.

The dynamics of $\langle\hat{a}(t)\rangle$ is determined by the interplay between the direct coherence exchange between vibrational modes through ζ_{SA} and their common coupling to the antenna through g_{S} and g_{A}. As a result of these coupling dynamics, the evolution equations confirm the pronounced drop in $T_{\mathrm{FID,A'(1)}}$ when the antenna is tuned to resonance with the A'(1) mode, which corresponds to a Purcell increase of the A'(1) relaxation rate by $4g_{\mathrm{S}}^2/\kappa_{\mathrm{ant}}\gamma_{\mathrm{S}}$ (4, 5). A numerical solution also captures the second, weaker reduction of the A'(1) decay time when the antenna is resonant with the effective A'(E) mode. This weak but clearly discerned second dip is a direct consequence of the Purcell-enhanced relaxation of A'(E) by $4g_{\mathrm{A}}^2/\kappa_{\mathrm{ant}}\gamma_{\mathrm{A}}$, as the antenna field is resonant with its lower-frequency vibrational mode. If the vibrational modes were fully uncoupled ($\zeta_{\mathrm{SA}} = 0$), there would be no pathway for the Purcell-accelerated relaxation of the A'(E) mode to influence the long-time dynamics of the laser-driven $A'(1)$ mode coherence. The intrinsic intramolecular vibrational interaction thus opens an additional antenna-dependent relaxation channel for the A'(1) mode, which ultimately gives rises to a second T_{FID} dip at the $A'(E)$ resonance. This effective dynamical cross-coupling between the A'(1) and A'(E) vibrational modes must compete with the bare vibrational relaxation pathways parametrized by the rates γ_{S} and γ_{A}, respectively. Therefore, although in principle we would also expect a second dip in T_{FID} when the laser drives the A'(E) mode and the antenna is resonant with the A'(1) frequency, the shorter intrinsic lifetime of the A'(E) mode does not allow for the cross-coupling to be observed. Therefore, the second drop in T_{FID} at the A'(1) frequency is not resolved in Fig. 4b of the main text. In the model the second dip at A'(1) is only visible if unreasonably high intramolecular ζ_{SA} or vibration-antenna coupling g_S constants are assumed.

Analytical derivation of $1/T_{\rm FID}$. In order to describe the vibrational and antenna frequency dependence of $T_{\rm FID}$, we derive an analytical expression for $T_{\rm FID}$ as follows. We write the equations of motion for the antenna and vibrational coherences [Eqs. (8) to (10)] for the Hamiltonian in Eq. (2) in matrix form as

$$\dot{\mathbf{Y}}(t) = -\mathbf{M}\,\mathbf{Y}(t) + \mathbf{F}(t), \tag{11}$$

where the mean-field vector $\mathbf{Y} = [\langle \hat{B}_{\rm S}\rangle, \langle \hat{a}\rangle, \langle \hat{B}_{\rm A}\rangle]^{\rm T}$ describes the coupled evolution of vibrational and antenna coherences and $\mathbf{M}$ is the dynamical matrix given by

$$\mathbf{M} = \begin{pmatrix} \gamma_{\rm S}/2 + i\omega_{\rm S} & ig_{\rm S} & i\zeta_{\rm SA} \\ ig_{\rm S} & \kappa_{\rm ant}/2 + i\omega_{\rm ant} & ig_{\rm A} \\ i\zeta_{\rm SA} & ig_{\rm A} & \gamma_{\rm A}/2 + i\omega_{\rm A} \end{pmatrix}. \tag{12}$$

We derive an analytical expression that describes the contributions of each type of coupling. We look for small deviations of the roots of dynamical matrix $\mathbf{M}$ in the form $\lambda = \gamma_{\rm S}/2 + i\omega_{\rm S} + \delta$, where δ is a complex number that encodes the changes in frequency and decay rate of the symmetric oscillator due to cavity coupling. First, we consider the free-cavity scenario ($g_{\rm S} = g_{\rm A} = 0$), i.e., Purcell effect due to intramolecular coupling between symmetric A'(1) and effective asymmetric A'(E) modes. Thus, we find that the symmetric vibrational decay rate reads

$$\frac{1}{T^0_{\rm FID}} = \frac{\gamma_{\rm S}}{2} + \frac{2\zeta^2_{\rm SA}\Delta\gamma}{(\Delta\gamma)^2 + 4\Delta^2_{\rm SA}}, \tag{13}$$

where $\Delta\gamma \equiv \gamma_{\rm A} - \gamma_{\rm S}$ and $\Delta_{\rm SA} = \omega_{\rm A} - \omega_{\rm S}$.

Similarly, in the simplest light-matter interaction scenario, i.e., no intramolecular coupling ($\zeta_{\rm SA} = 0$), the cavity only couples to one of the vibrational modes ($g_{\rm A} = 0$). Considering the bad cavity limit $\kappa_{\rm ant} \gg \gamma_{\rm S}$ (bare Purcell enhancement), the second contribution to the vibrational decay rate is given by

$$\mathrm{Re}[\delta] = \frac{1}{2T_{1,\rm P}} = \frac{2g^2_{\rm S}\Delta\Gamma}{(\Delta\Gamma)^2 + 4\Delta^2_{\rm aS}}, \tag{14}$$

where $\Delta\Gamma \equiv \kappa_{\rm ant} - \gamma_{\rm S}$ is the antenna-vibration decay mismatch and $\Delta_{\rm aS} = \omega_{\rm ant} - \omega_{\rm S}$ is the detuning from the symmetric mode (5).

Third, when the cavity also couples to the asymmetric mode, a reduction of the decay time $T_{\rm FID}$ is expected due to the Purcell effect. Therefore, even if the symmetric mode is uncoupled from the cavity ($g_{\rm S} = 0$), we expect to have an effective cavity frequency dependent lifetime via the Purcell-enhanced decay rate $\gamma_{\rm A}$. Hence, we can simply insert the Purcell enhancement of the asymmetric decay rate [Eq.(14) for asymmetric mode ($S \to A$)] into the intramolecular expression [Eq. (13)], which gives as a result

$$\mathrm{Re}[\delta] = \frac{1}{2T_{1,\rm IVR-P}} = \frac{4\zeta^2_{\rm SA}[\Delta\gamma + 4g^2_{\rm A}(\kappa_{\rm ant} - \gamma_{\rm A})/((\kappa_{\rm ant} - \gamma_{\rm A})^2 + \Delta^2_{\rm aA})]}{[\Delta\gamma + 4g^2_{\rm A}(\kappa_{\rm ant} - \gamma_{\rm A})/((\kappa_{\rm ant} - \gamma_{\rm A})^2 + \Delta^2_{\rm aA})]^2 + 4\Delta^2_{\rm aS}}. \tag{15}$$

In the bad cavity limit $\kappa_{\rm ant} \gg \gamma_{\rm A}$, therefore $\kappa_{\rm ant} - \gamma_{\rm A} \approx \kappa_{\rm ant}$ and the factor $4g^2_{\rm A}\kappa_{\rm ant}/(4\Delta^2_{\rm aA} + \kappa^2_{\rm ant})$ is smaller than $\Delta\Gamma$. Thus, we can expand Eq. (15) up to first order to obtain [Eq. (3) in main text]

$$\frac{1}{2T_{1,\rm IVR-P}} \approx \frac{\gamma_{\rm S}}{2} + \frac{4\zeta^2_{\rm SA}g^2_{\rm A}\kappa_{\rm ant}}{[(\Delta\gamma)^2 + 4\Delta^2_{\rm SA}][\kappa^2_{\rm ant} + 4\Delta^2_{\rm aA}]}, \tag{16}$$

with $\Delta_{\rm aA} = \omega_{\rm ant} - \omega_{\rm A}$. The last contribution is due to cavity-mediated interaction between vibrational modes, i.e, $\zeta_{\rm SA}/\kappa_{\rm ant} \to 0$. Under this approach, we expect cavity-mediated surrogate coupling between the symmetric and effective asymmetric modes, as the dynamical matrix becomes equivalent to the electromagnetic induced transparency (EIT) Hamiltonian from AMO physics (7). Hence, we obtain [Eq. (4) in main text]

$$\mathrm{Re}[\delta] = \frac{1}{2T_{1,\rm anti-P}} = -\eta\,\mathrm{Re}\left\{\frac{g^2_{\rm S}[\Delta\gamma/2 + i\Delta_{\rm SA}]}{g^2_{\rm A} + g^2_{\rm S} - [\Delta\gamma/2 + i\Delta_{\rm SA}][\Delta\Gamma/2 - i\Delta_{aS}]}\right\}, \tag{17}$$

where $0 < \eta < 1$ is an arbitrary weighting factor. Equation (17) can be seen as an anti-Purcell contribution to the decay time $T_{\rm FID,A'(1)}$ of the symmetric mode.

Finally, the total vibrational decay time for the symmetric mode can be written as

$$1/T_{\rm FID,A'(1)} \approx 1/T^0_{\rm FID} + 1/2T_{1,\rm P} + 1/2T_{1,\rm IVR-P} + 1/2T_{1,\rm anti-P}, \tag{18}$$

which corresponds to Eq. (2) in main text.

In a similar form, an expression for the asymmetric mode can be also derived and given by

$$\begin{aligned}\frac{1}{T_{\rm FID,A}} \;=\; & \frac{\gamma_{\rm A}}{2} - \frac{2\zeta^2_{\rm SA}\Delta\gamma}{(\Delta\gamma)^2 + 4\Delta^2_{\rm SA}} + \frac{2g^2_{\rm A}\Delta\Gamma_{\rm A}}{(\Delta\Gamma_{\rm A})^2 + 4\Delta^2_{\rm aA}} + \frac{4\zeta^2_{\rm SA}g^2_{\rm S}\kappa_{\rm ant}}{[(\Delta\gamma)^2 + 4\Delta^2_{\rm SA}][\kappa^2_{\rm ant} + 4\Delta^2_{\rm aS}]} \\ & + \eta\,\mathrm{Re}\left\{\frac{g^2_{\rm A}[\Delta\gamma/2 + i\Delta_{\rm SA}]}{g^2_{\rm A} + g^2_{\rm S} - [\Delta\gamma/2 + i\Delta_{\rm SA}][\Delta\Gamma/2 + i\Delta_{\rm aA}]}\right\}\end{aligned} \tag{19}$$

with $\Delta\Gamma_{\rm A} = \kappa_{\rm ant} - \gamma_{\rm A}$. Equations (18) and (19) are plotted in Fig. 4a and 4b in the main text, respectively.

References

1. R Adato, S Aksu, H Altug, Engineering mid-infrared nanoantennas for surface enhanced infrared absorption spectroscopy. *Mater. Today* **18**, 436–446 (2015).
2. DE Rosenfeld, Z Gengeliczki, BJ Smith, TDP Stack, MD Fayer, Structural Dynamics of a Catalytic Monolayer Probed by Ultrafast 2D IR Vibrational Echoes. *Science* **334**, 634–639 (2011).
3. C Yan, et al., Unraveling the dynamics and structure of functionalized self-assembled monolayers on gold using 2D IR spectroscopy and MD simulations. *Proc. Natl. Acad. Sci.* **113**, 4929–4934 (2016).
4. B Metzger, et al., Purcell-Enhanced Spontaneous Emission of Molecular Vibrations. *Phys. Rev. Lett.* **123**, 153001 (2019).
5. JF Triana, et al., Semi-empirical quantum optics for mid-infrared molecular nanophotonics. *J. Chem. Phys.* **156**, 124110 (2022).
6. HP Breuer, Non-Markovian generalization of the Lindblad theory of open quantum systems. *Phys. Rev. A - At. Mol. Opt. Phys.* **75**, 1–9 (2007).
7. M Fleischhauer, A Imamoglu, JP Marangos, Electromagnetically induced transparency: Optics in coherent media. *Rev. Mod. Phys.* **77**, 633–673 (2005).